

Marangoni-driven freezing dynamics of supercooled binary droplets

Feng Wang,¹ Hao Zeng,¹ Yihong Du,¹ Xinyu Tang,¹ and Chao Sun^{1,2,3,*}

¹*New Cornerstone Science Laboratory, Center for Combustion Energy,
Key Laboratory for Thermal Science and Power Engineering of Ministry of Education,*

Department of Energy and Power Engineering, Tsinghua University, 100084 Beijing, China

²*Department of Engineering Mechanics, School of Aerospace Engineering, Tsinghua University, Beijing 100084, China*

³*Physics of Fluids Group, Max Planck Center for Complex Fluid Dynamics,
and J.M.Burgers Center for Fluid Dynamics, University of Twente, 7500 AE Enschede, The Netherlands*

(Dated: July 31, 2024)

Solidification of droplets is of great importance to various technological applications, drawing considerable attention from scientists aiming to unravel the fundamental physical mechanisms. In the case of multicomponent droplets undergoing solidification, the emergence of concentration gradients may trigger significant interfacial flows that dominate the freezing dynamics. Here, we experimentally investigate the fascinating snow-globe freezing dynamics of supercooled ethanol-water droplets. We reveal that these unique freezing dynamics are driven by solidification-induced solutal Marangoni flow within the droplets. We quantitatively characterize the concentration-dependent migration and growth dynamics of ice particles, tightly connecting them to the solutal Marangoni effect and the associated convective heat transfer. Moreover, we show that the final wrapping state of droplets can be modulated by the concentration of ethanol. Our findings may pave the way for novel insights into the physicochemical hydrodynamics of multicomponent liquids undergoing phase transitions.

Solidification of droplets is ubiquitous in both natural environments and industrial applications. The accumulation of frozen droplets on artificial surfaces can lead to a range of detrimental consequences to aviation safety [1], maritime operations [2] and wind turbines [3] in the cold regions. Substantial efforts have been dedicated to enhancing our understanding of the intricate dynamics of ice crystal nucleation and growth during solidification [4–6], covering a wide array of factors, such as the influence of environmental medium [7–9], the inertia of droplets [10–12], the composition of droplets [13–15], and the characteristics of substrates [16–18].

The freezing dynamics of supercooled droplets on surfaces is significantly different from that of warm droplets (at room temperature) on cold surfaces. For the case of warm pure water droplets, a uni-directional advancing ice front away from the cold substrate was observed [19], due to the dominant heat conduction through the ice phase to consume the release of latent heat during solidification. In contrast, dendritic freezing dynamics along the substrate was characterized during the solidification of supercooled water droplets deposited on a cold wall [20], which should consider the heat conduction in both the supercooled liquid and the neighboring solid substrate. In the case of warm saline droplets, the freezing dynamics were similar to those of warm pure water droplets, with a slight difference in the tip angle formed at the top of the droplets [21], due to the volume expansion during solidification [19]. Conversely, an unexpected interfacial ice sprouting dynamics was reported during the solidification of supercooled saline droplets [22], which resulted from the formation of a brine film during the nucleation and recalescence process accompanied by salt rejection.

More interestingly, if the rejected compositions near the ice front can significantly change surface tension, a

strong solutal Marangoni effect can be expected within the droplets, and this may further influence the freezing dynamics of the droplets. Based on this idea, Wang *et al.* reported the self-lifting freezing dynamics of warm ethanol-water droplets on a cold substrate [23]. The upward solutal Marangoni flow within droplets is observed, driven by the localized enrichment of ethanol near the advancing ice front. As a consequence, the pronounced dynamic growth angle at the tri-junction of liquid-solid-gas interfaces is characterized, leading to a nearly doubling of the final height of the droplets due to the geometrical relationship [24].

Then, the remaining question is: what will happen during the solidification of supercooled ethanol-water droplets on cold surface? The ice crystal growth dynamics accompanied by ethanol rejection may involve more complex physical phenomena than salt-induced effects, because the presence of Marangoni flow can significantly enhance the convective heat transfer and mass transport characteristics, and consequently result in novel freezing dynamics of supercooled ethanol-water droplets.

In this Letter, we investigate experimentally the fascinating migration and growth dynamics of ice particles at the interface of supercooled ethanol-water droplets. This phenomenon is propelled by solutal Marangoni flow [23], which arises from the localized enrichment of ethanol near the ice front [25]. Our findings reveal that the unique dynamics of ice particles, characterized by a constant migration velocity and constant growth rate, can be well elucidated by incorporating the solutal Marangoni effect and the associated convective heat transfer. This novel freezing process culminates in the formation of beautiful snow-globe-like patterns [26], the distinctive dimensions of which are found to depend on the concentration of ethanol.

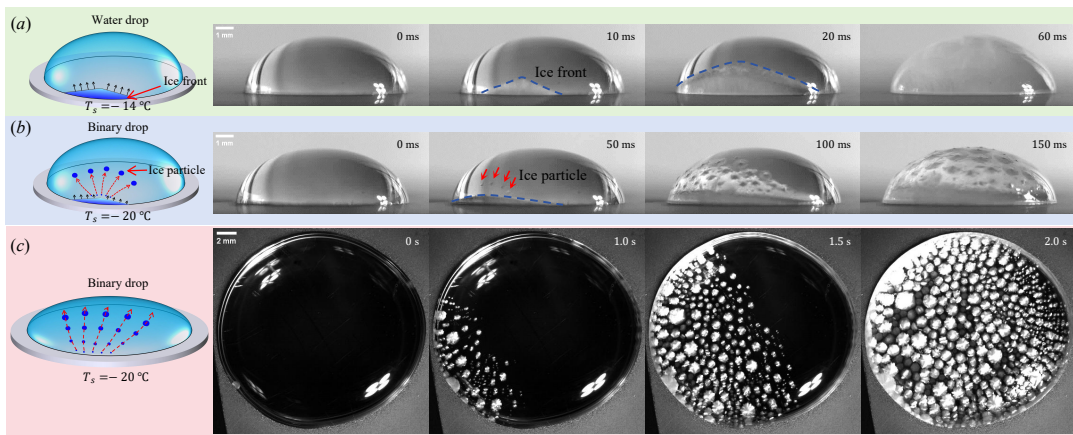


FIG. 1. Freezing dynamics of supercooled droplets on cold surfaces. **(a)** Side view for recalescence of the supercooled water droplets ($V_0 = 150 \mu\text{L}$, $T_s = -14 \text{ }^\circ\text{C}$). **(b)** Side view for ice migration of the supercooled ethanol-water droplets ($c_0 = 0.05$, $V_0 = 150 \mu\text{L}$, $T_s = -20 \text{ }^\circ\text{C}$). **(c)** Top-down view for ice migration and growth of the supercooled ethanol-water droplets ($c_0 = 0.20$, $V_0 = 500 \mu\text{L}$, $T_s = -20 \text{ }^\circ\text{C}$). In snapshots, the blue dash line represents the ice-water interface, and the red arrows mark ice particles. The red dash line in sketches indicates the trajectories of ice particles.

Observation of the snow-globe dynamics. In the experiments, ethanol-water droplets with various volume (V_0) and volume fraction of ethanol (c_0) are gently deposited onto a nickel-plated copper substrate inside a self-built transparent environmental chamber at room temperature ($T_0 = 25 \text{ }^\circ\text{C}$). Then, the substrate is slowly cooled by an embedded peltier cooler down to $T_s = -20 \text{ }^\circ\text{C}$, and the droplet is gradually cooled into a supercooled state before the suddenly nucleation of ice crystal [22]. The freezing dynamics are recorded by high-speed cameras (Photron Nova S12) from both the top-down view and side view, and the temperature evolution is recorded by an IR camera (Telops FAST L200, Stirling-cooled MCT detector) from the top-down view.

Figure 1 presents the typical freezing dynamics of supercooled droplets (Movie S1). For a pure water droplet ($V_0 = 150 \mu\text{L}$, Fig. 1a), the rapid recalescence process is observed, with a typical advancing velocity of dendritic ice front at the order of 10 cm/s , which is consistent with previous studies [20]. However, in the case of a binary ethanol-water droplet ($V_0 = 150 \mu\text{L}$, $c_0 = 0.05$, Fig. 1b), the initial formation of dendritic ice front is observed, as indicated by the blue dash line in Fig. 1b. Surprisingly, some ice particles are observed to move away from the ice front (as marked by the red arrows), towards the opposite side of droplets along an almost straight line (as indicated by the red dash line in the sketch of Fig. 1b). These ice particles move at a higher velocity than the advancing ice front. Besides, the amount and size of ice particles gradually increase, which is reminiscent of the snow-globe effect observed in nature and during the solidification of soap bubbles [26]. Moreover, this observed snow-globe freezing dynamics of supercooled ethanol-water droplets is much slower than the recalcitrant freezing dynamics of supercooled water droplets, suggesting that there is a

different underlying physical mechanism.

This fascinating snow-globe-like dynamics is still observed when the volume and concentration of the droplet are increased ($V_0 = 500 \mu\text{L}$, $c_0 = 0.20$, Fig. 1c). From the top-down view (Movie S2), the trajectory and the size of ice particles at the interface of supercooled ethanol-water droplets can be tracked much better. Distinct from the dense and continuous ice patterns formed after the recalescence process of supercooled pure water droplets [27] and supercooled saline droplets [28], hundreds of small dispersed ice particles nucleate progressively, grow slowly and migrate unidirectionally from one side to the other side, and ultimately cover the entire interface of the supercooled ethanol-water droplet.

Global characteristics of the snow-globe dynamics. In order to understand the mechanism of the snow-globe freezing dynamics, we first utilize the thermal camera to investigate the global characteristics of temperature evolution at the interface of supercooled droplets (Movie S3), as shown in Fig. 2. The initial temperature of droplets (T_{liq}) is far below the freezing point (T_m), confirming the supercooled state of droplets. Due to the release of latent heat during the ice formation process, the local temperature near the ice particles increases rapidly to the phase change temperature ($T_{ice} = T_m$).

For the supercooled water droplets, the evolution of typical thermal pattern is almost axis-symmetric (Fig. 2a). By transforming the temperature profile along the x direction (as marked by the dash line in Figs. 2a) into a spatio-temporal phase diagram (Fig. 2c), the axis-symmetric recalescence process of the supercooled pure water droplets could be more straightforward, due to the symmetry of this diagram. Furthermore, the typical velocity $v_x = 7.6 \text{ cm/s}$ can be obtained by calculating the slope of temperature contours, which is consistent with

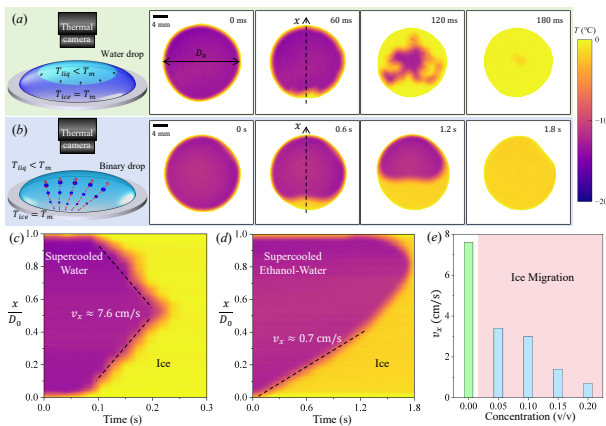


FIG. 2. Thermal snapshots of supercooled droplets on cold surfaces. Top-down view for (a) supercooled water droplets ($V_0 = 500 \mu\text{L}$, $T_s = -14 \text{ }^\circ\text{C}$), and (b) supercooled ethanol-water droplets ($c_0 = 0.20$, $V_0 = 500 \mu\text{L}$, $T_s = -20 \text{ }^\circ\text{C}$). Evolution of ice-liquid interfaces for (c) supercooled water droplets, and (d) supercooled ethanol-water droplets, along x direction as defined by the dash line in (a,b). (e) The typical velocity v_x obtained from thermal imaging, which is determined by the slope in (c,d) as indicated by the dash line. (a-d) are in the same color bar.

the observed advancing velocity of the ice front by high-speed cameras (Fig. 1a).

In contrast, the evolution of typical thermal pattern is quite unidirectional for the supercooled ethanol-water droplets ($c_0 = 0.20$, Fig. 2b). The warm region (ice phase) gradually invades the cold region (supercooled ethanol-water phase) along the x direction, as marked by the dash line in Figs. 2b. Similarly, the typical velocity $v_x = 0.7 \text{ cm/s}$ can be calculated from the spatio-temporal phase diagram (Fig. 2d), which is an order of magnitude smaller than that of the supercooled water droplets.

Moreover, we perform a series of temperature measurements for various concentrations (c_0). A pronounced decrease in the concentration-dependence of the typical velocity v_x is characterized, suggesting a concentration-related physical mechanism to dominate the snow-globe freezing dynamics of supercooled ethanol-water droplets.

Marangoni-driven migration of ice particles. By tracing the position (x, y) of ice particles, we calculate the distance of ice particle migration $\xi = \sqrt{(x - x_0)^2 + (y - y_0)^2}$, as sketched in Fig. 3a, where (x_0, y_0) is the initial position of the ice particle. Qualitatively, the migration distance is found to be proportional to time $\xi \sim t$ as shown in Fig. 3b, indicating a constant migration velocity $v_{ice} = \text{const}$. Moreover, the migration velocity v_{ice} is found to decrease with the concentration of ethanol c_0 , which is consistent with the tendency of the observed typical velocity v_x by thermal imaging (Fig. 2e).

Based on the concentration-dependence of the migration velocity v_{ice} , we propose a Marangoni-driven mechanism for the migration dynamics of ice particles, as

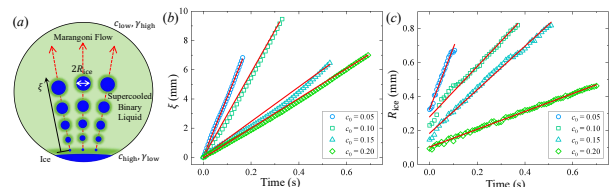


FIG. 3. Ice particle dynamics of supercooled binary droplets. (a) Top-down view for the sketch of ice growth and migration induced by the solutal Marangoni effect. The green shadow indicates the concentration distribution. Ethanol is enriched near the ice front c_{high} , which causes the decrease of local surface tension γ_{low} . This freezing-induced surface tension gradient produces solutal Marangoni flow towards the unfrozen part of droplets, and it drives the migration and growth of ice particles. (b) Migration distance of ice particle ξ increases linearly with time t . (c) Radius of ice particles R_{ice} increases linearly with time t . The red solid line represents the best linear fit of experimental dots.

sketched in Fig. 3a. During solidification of supercooled ethanol-water droplets, the local concentration of ethanol c_{high} in the vicinity of the ice front increases, and becomes higher than the concentration away from the ice front c_{low} . Consequently, the surface tension γ_{low} near the ice front is smaller than that away from the ice front γ_{high} , which triggers the solutal Marangoni flow across the droplet and drives ice particles to move. Thus, the dimensionless migration velocity of ice particles v_{ice}/v_{diff} can be described by the solutal Marangoni number Ma [29],

$$\frac{v_{ice}}{v_{diff}} \sim Ma, \quad (1)$$

where D, μ are the mass diffusivity and viscosity of liquids, D_0 is the diameter of the droplet, $v_{diff} = D/D_0$ is the typical molecular diffusion velocity, $Ma = \Delta\gamma D_0/(\mu D)$ is the solutal Marangoni number, $\Delta\gamma = \gamma_0 - \gamma_{sat}$ is the typical surface tension difference between the initial state γ_0 which is determined by the initial concentration c_0 , and the saturated state γ_{sat} which is determined by the substrate temperature T_s .

For a given substrate temperature ($T_s = -20 \text{ }^\circ\text{C}$), surface tension at the saturated state γ_{sat} is almost constant, while surface tension at the initial state γ_0 decreases with concentration c_0 (Supplemental Material). Thus, the typical surface tension difference $\Delta\gamma$ decreases with concentration c_0 , and consequently the migration velocity of ice particles V_{ice} decreases with concentration c_0 .

Marangoni-driven convective growth of ice particles. Besides, we track the evolution of individual area (S) of ice particles, and calculate the equivalent radius of ice particles $R_{ice} = \sqrt{S/\pi}$. Figure 3c presents the growth dynamics of ice particles at the interface of supercooled binary droplets. The radius of ice particles increases linearly with time $R_{ice} \sim t$, indicating a constant growth

rate of particle radius $v_{grow} = \text{const}$, which is obviously different from the diffusive growth of ice front $R_{ice} \sim \sqrt{t}$ in previous studies [30]. Furthermore, the growth rate of ice particles v_{grow} is found to also decrease with concentration c_0 .

Since the solutal Marangoni effect is crucial to the migration dynamics of ice particles, we should take account of the associated Marangoni-driven convective heat transfer effect on the growth dynamics of ice particles. Following the thermal analysis on evaporating droplets in previous work [31], the released latent heat due to ice formation Q_L can be expressed as follows,

$$Q_L \sim \rho L_f v_{grow}, \quad (2)$$

where ρ and L_f are the density of liquids and the latent heat of solidification, respectively.

The convective heat flux Q_c induced by solutal Marangoni flow V_M can be expressed as follows,

$$Q_c \sim \rho c_p V_M \Delta T \sim \rho c_p V_M (T_s - T_m), \quad (3)$$

where c_p is the specific heat capacity of liquid, $\Delta T = T_s - T_m$ is the typical temperature difference between the substrate temperature T_s and the freezing point T_m .

By balancing these two heat fluxes $Q_L = Q_c$ (Eq. 2 and 3), the dimensionless growth rate of ice particles v_{grow}/v_{diff} can be described by the combination of the solutal Marangoni number Ma and the Stefan number St ,

$$\frac{v_{grow}}{v_{diff}} \sim Ma \cdot St, \quad (4)$$

where $St = c_p \Delta T / L_f$ is the Stefan number [32].

According to Eq. 4, the growth rate of ice particles v_{ice} is proportional to the solutal Marangoni velocity V_M and the supercooling temperature ΔT , which holds almost constant during one specific experiment. Moreover, for a given substrate temperature ($T_s = -20$ °C), the increase of concentration c_0 can lead to not only the decrease of solutal Marangoni velocity V_M , but also the decrease of supercooling temperature $\Delta T = T_s - T_m$. Therefore, the growth rate of ice particles v_{grow} is expected to decrease more drastically with concentration c_0 , compared with the migration velocity v_{ice} (Eq. 1).

Comparisons between experiments and models. Quantitatively, the scaling relations predicted by physical models for the migration and growth dynamics of ice particles (Eq. 1 and Eq. 4), show great agreements with the experimental data obtained from both the high-speed imaging and thermal imaging (Fig. 1,2). The dimensionless migration velocity of ice particles v_{ice}/v_{diff} is proportional to the solutal Marangoni number Ma (Fig. 4a), reflecting the Marangoni-driven migration mechanism of ice particles. The dimensionless growth rate of ice particles v_{grow}/v_{diff} is proportional to the combination of

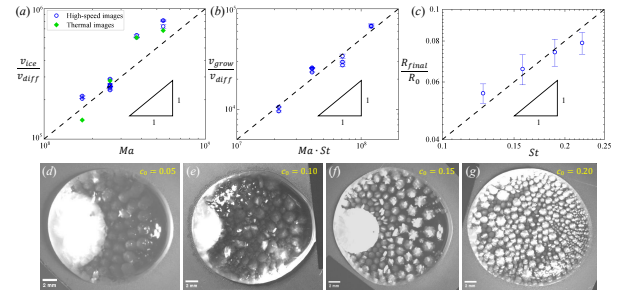


FIG. 4. Physical model for ice growth and migration. (a) Scaling relation for ice migration velocity v_{ice} versus the solutal Marangoni number Ma . (b) Scaling relation for ice particle growth rate v_{grow} versus the combination of the solutal Marangoni number Ma and the Stefan number St . (c) Scaling relation for the radius of ice particles at the end of migration R_{final} versus the Stefan number St . (d-g) Snapshots from the top-down view at the end of migration at difference concentration c_0 . The blue circle represents the experimental data obtained from high-speed cameras, and the green diamond represents the experimental data obtained from thermal camera. The error bar in (a-c) for the standard deviation of at least ten measurements.

the solutal Marangoni number Ma and the Stefan number St (Fig. 4b), highlighting the Marangoni-driven convective growth mechanism at the interface of supercooled ethanol-water droplets.

Furthermore, based on our understanding of ice particle dynamics, we now focus on the final patterns of freezing supercooled ethanol-water droplets when the droplet is fully covered by dispersed ice particles, as shown in Fig. 4d-g. With the increase of concentration c_0 , the ice particle becomes smaller and thicker, which can be inferred from the brightness of ice particles. The dependence of final patterns on concentration c_0 can be explained by considering the characteristic timescale τ_c for ice particles travelling across the droplets, $\tau_c \sim R_0/v_{ice}$, where $R_0 \approx 1$ cm is the initial radius of droplet in experiments for all c_0 . Then, the dimensionless radius of ice particles at the final state R_{final}/R_0 can be expressed as follows,

$$\frac{R_{final}}{R_0} \sim \frac{\tau_c \cdot v_{grow}}{R_0} \sim St. \quad (5)$$

Surprisingly, according to Eq. 5, the final size of ice particles is found to be independent of the solutal Marangoni flow, and is solely determined by the supercooling temperature ΔT which should take account of the depression effect on freezing point T_f of ethanol concentration c_0 (Supplement Material). Figure 4c presents the comparison between the experimental data and the predictions of the simple model, indicating that the model captures the dependence of ice particle radius at final state on concentration c_0 . Besides, the characteristic timescale τ_c increases with concentration c_0 , and the

thickness of ice particles is expected to obey the diffusive growth dynamics $h \sim \sqrt{\tau_c}$ [30]. Therefore, the ice particles become thinner and consequently more transparent with the decrease of concentration c_0 .

In conclusion, we present a compelling study on the freezing dynamics of supercooled ethanol-water droplets, revealing the underlying mechanisms that drive the observed snow-globe-like dynamics and patterns. These intriguing phenomena are traced back to the internal solutal Marangoni flow, triggered by the localized enriched concentration of ethanol near the ice front. By incorporating the effects of solutal Marangoni flow and the associated convective heat transfer, we have developed physical models that quantitatively capture the migration and growth dynamics of ice particles at the droplet-air interface. Our findings may advance the fundamental understanding of the complex physicochemical hydrodynamics in the context of multicomponent liquids undergoing phase transitions and may further pave the way for droplet-based technological innovations in manufacturing and material science[29].

This work has been supported by the Natural Science Foundation of China under Grant No. 11988102, the National Key R&D Program of China under Grant No. 2021YFA0716201, the New Cornerstone Science Foundation through the New Cornerstone Investigator Program and the XPLOER PRIZE, the Postdoctoral Fellowship Program of the China Postdoctoral Science Foundation under Grant Nos. GZB20240366 and 2024M751637, and Shuimu Tsinghua Scholar Program under Grant No. 2023SM038.

* chaosun@tsinghua.edu.cn

- [1] T. Cebeci and F. Kafyeke, *Annu. Rev. Fluid Mech.* **35**, 11 (2003).
- [2] A. Deghani-Sanij, S. Deghani, G. Naterer, and Y. Muzychka, *Ocean Eng.* **132**, 25 (2017).
- [3] L. Makkonen, T. Laakso, M. Marjaniemi, and K. Finstad, *Wind Eng.* **25**, 3 (2001).
- [4] P. Kant, R. Koldewej, K. Harth, M. van Limbeek, and D. Lohse, *Proc. Natl. Acad. Sci.* **117**, 2788 (2020).
- [5] R. Koldewej, P. Kant, K. Harth, R. de Ruiter, H. Gelderblom, J. Snoeijer, D. Lohse, and M. van Limbeek, *Phys. Rev. Fluids* **6**, L121601 (2021).
- [6] R. Grivet, A. Monier, A. Huerre, C. Josserand, and T. Séon, *Phys. Rev. Lett.* **128**, 254501 (2022).
- [7] S. Lyu, X. Zhu, D. Legendre, and C. Sun, *Droplet* **2**, e90 (2023).
- [8] H. Lambley, G. Graeber, R. Vogt, L. Gaugler, E. Baumann, T. Schutzius, and D. Poulidakos, *Nature Phys.* **19**, 649 (2023).
- [9] G. Graeber, T. Schutzius, H. Eghlidi, and D. Poulidakos, *Proc. Natl. Acad. Sci.* **114**, 11040 (2017).
- [10] M. Hu, F. Wang, Q. Tao, L. Chen, and D. Rubinstein, S. and Deng, *Phys. Rev. Fluids* **5**, 081601 (2020).
- [11] V. Thiévenaz, T. Séon, and C. Josserand, *J. Fluid Mech.* **874**, 756 (2019).
- [12] V. Thiévenaz, C. Josserand, and T. Séon, *Phys. Rev. Fluids* **5**, 041601 (2020).
- [13] H. Zeng, Y. Wakata, X. Chao, M. Li, and C. Sun, *J. Colloid Interface Sci.* **648**, 736 (2023).
- [14] Y. Jiang, Y. Zhao, H. Zhang, C. Yang, and P. Cheng, *Cell Rep. Phys. Sci.* **5** (2024).
- [15] S. Kharal and J. Louf, *Langmuir* **40**, 118 (2023).
- [16] V. Lolla, S. Ahmadi, H. Park, A. Fugaro, and J. Boreyko, *Phys. Rev. Lett.* **129**, 074502 (2022).
- [17] F. Wang, L. Chen, Y. Li, X. Gu, P. Huo, M. Hu, and D. Deng, *Phys. Fluids* **35** (2023).
- [18] J. de Ruiter, D. Soto, and K. Varanasi, *Nature Phys.* **14**, 35 (2018).
- [19] A. Marin, O. Enriquez, P. Brunet, P. Colinet, and J. Snoeijer, *Phys. Rev. Lett.* **113**, 054301 (2014).
- [20] M. Schremp, J. Campbell, H. Christenson, and C. Tropea, *Langmuir* **33**, 4870 (2017).
- [21] F. Boulogne and A. Salonen, *Appl. Phys. Lett.* **116** (2020).
- [22] F. Chu, S. Li, C. Zhao, Y. Feng, Y. Lin, X. Wu, X. Yan, and N. Miljkovic, *Nature Commun.* **15**, 2249 (2024).
- [23] F. Wang, L. Chen, Y. Li, P. Huo, X. Gu, M. Hu, and D. Deng, *Phys. Rev. Lett.* **132**, 014002 (2024).
- [24] D. Anderson, M. Worster, and S. Davis, *J. Cryst. Growth* **163**, 329 (1996).
- [25] D. Dedovets, C. Monteux, and S. Deville, *Science* **360**, 303 (2018).
- [26] S. Ahmadi, S. Nath, C. Kingett, P. Yue, and J. Boreyko, *Nature Commun.* **10**, 2531 (2019).
- [27] Z. Zhu, X. Zhang, Y. Zhao, X. Huang, and C. Yang, *Int. J. Therm. Sci.* **171**, 107241 (2022).
- [28] S. Singha, P. Das, and B. Maiti, *Langmuir* **34**, 9064 (2018).
- [29] D. Lohse and X. Zhang, *Nature Rev. Phys.* **2**, 426 (2020).
- [30] E. Ghabache, C. Josserand, and T. Séon, *Phys. Rev. Lett.* **117**, 074501 (2016).
- [31] B. Reichert, J. Le Cam, A. Saint-Jalmes, and G. Pucci, *Phys. Rev. Lett.* **127**, 144501 (2021).
- [32] H. Zeng, S. Lyu, D. Legendre, and C. Sun, *Phys. Rev. Fluids* **7**, 103605 (2022).